Direct laser acceleration of electrons assisted by strong laser-driven azimuthal plasma magnetic fields

Z. Gong (弓正),[1,2] F. Mackenroth,[3,4] T. Wang (王涛),[4] X. Q. Yan,[1] T. Toncian,[5] and A. V. Arefiev[4,*]

[1]*SKLNPT, KLHEDP and CAPT, School of Physics, Peking University, Beijing 100871, China*

[2]*Center for High Energy Density Science, The University of Texas at Austin, Austin, Texas 78712, USA*

[3]*Max Planck Institute for the Physics of Complex Systems, 01187 Dresden, Germany*

[4]*Department of Mechanical and Aerospace Engineering, University of California San Diego, La Jolla, California 92093, USA*

[5]*Institute for Radiation Physics, Helmholtz-Zentrum Dresden-Rossendorf e.V., 01328 Dresden, Germany*

(Received 1 November 2018; revised 25 May 2020; accepted 9 June 2020; published 13 July 2020)

A high-intensity laser beam propagating through a dense plasma drives a strong current that robustly sustains a strong quasistatic azimuthal magnetic field. The laser field efficiently accelerates electrons in such a field that confines the transverse motion and deflects the electrons in the forward direction. Its advantage is a threshold rather than resonant behavior, accelerating electrons to high energies for sufficiently strong laser-driven currents. We study the electron dynamics via a test-electron model, specifically deriving the corresponding critical current density. We confirm the model's predictions by numerical simulations, indicating energy gains two orders of magnitude higher than achievable without the magnetic field.

DOI: 10.1103/PhysRevE.102.013206

I. INTRODUCTION

Recent advancements in high-power laser technology [1,2] have paved the way for multidisciplinary applications by enabling compact plasma-based sources of energetic particles (electrons [3], ions [4–6], positrons [7–10], and neutrons [11]) and radiation [12,13]. The energy transfer from the laser pulse to the plasma electrons is critically important for these applications, since energetic electrons are required to drive secondary particle and radiation sources. The applications that prioritize the monoenergetic feature of the electron spectrum tend to rely on the laser-wakefield acceleration [14–16], whereas the applications that prioritize the electron charge tend to rely on the direct laser acceleration regime [17,18]. The latter include bright, short-pulsed gamma-ray sources [19–31] that are necessary for advanced nuclear and radiological detection systems [32,33].

The essence of the direct laser acceleration is the energy transfer from the laser electric field directly to the electrons. This can take place in a dense plasma without stringent density limitations [34,35], which allows the laser to accelerate a large electron population. The regime can even be used to accelerate electrons in optically opaque plasmas if the laser is sufficiently intense to induce relativistic transparency [36,37].

Typically, the electrons accelerated by the laser beam are pulled into the beam from the surrounding plasma, so they acquire an initially transverse momentum, p_i, prior to the acceleration. The presence of this momentum can severely limit the electron energy gain. For example, if the initial momentum is relativistic, $p_i \gg m_e c$, then the energy gain of an electron in a plane electromagnetic wave with the normalized amplitude $a_0 \gg p_i/m_e c$ is inversely proportional to p_i [38]:

$$\varepsilon_0 = \gamma_0 m_e c^2 \approx \frac{a_0^2}{2}\frac{m_e c}{p_i} m_e c^2, \tag{1}$$

where m_e is the electron mass, c is the speed of light, and

$$\gamma_0 \approx \frac{a_0^2}{2}\frac{m_e c}{p_i}. \tag{2}$$

The normalized amplitude for a wave with intensity I_0 and wavelength λ_0 is $a_0 \approx 0.85 I_0[10^{18}\ \mathrm{W/cm^2}]^{1/2}\lambda_0[\mu\mathrm{m}]$. The observed suppression, $\gamma_0 \propto 1/p_i$, is due to the electron dephasing from the laser pulse [39].

Significant research has been dedicated to mitigating the negative impact of the dephasing in order to increase the electron energy gain [38,40–44]. The quasistatic electric fields caused by charge separation have been shown to alter the dephasing, which leads to an enhanced energy exchange between the electrons and the laser [45]. However, the mechanisms that involve the quasistatic plasma electric field imply that the corresponding force on the electrons is much stronger than the force generated by plasma magnetic fields.

In this paper, we consider a regime where plasma magnetic rather than electric field determines the dynamics of laser-accelerated electrons. This regime is naturally realized in laser-plasma interactions with a characteristic ion response time, $1/\omega_{pi}$, shorter or comparable to the duration of the laser pulse. The ions then have sufficient time to move and reduce the electric field, negating its impact. The regime with a dominant magnetic field can come into play as we either increase the laser pulse duration or increase the plasma density. An example of the latter would be the experiments

*aarefiev@eng.ucsd.edu

at ultrahigh laser intensities with solid density targets that become transparent as a result of the interaction. These experiments are projected to take place at the next generation laser facilities, such as ELI [46], Apollon [47], and XCELS [48], where the necessary intensities will become accessible.

Our goal is to find the conditions for effective electron acceleration by an intense laser pulse in the presence of a laser-driven quasistatic magnetic field. The magnetic field in this configuration is azimuthal. Intense laser beams drive longitudinal electron currents through the plasma, inducing such fields [49–53]. In contrast to the electric fields, azimuthal magnetic fields are robust with respect to the ion motion and can be sustained at ultrahigh intensities over the laser pulse duration.

We show that direct laser acceleration of electrons assisted by a strong plasma magnetic field can lead to a significant energy gain, provided that the plasma current density is sufficiently high. Using a test-electron model, we find that the corresponding critical current density scales linearly with a_0. The effect is confirmed using two- and three-dimensional particle-in-cell simulations (2D and 3D PIC) with detailed electron tracking. The advantage of the considered regime is that it can be employed to generate large numbers of high-energy electrons in an overdense plasma irradiated by an ultraintense laser. Such dense energetic bunches are the key to driving bright gamma-ray sources [26,54,55].

The rest of the paper consists of four sections. In Sec. II, we present a 3D particle-in-cell (PIC) simulation where a high-intensity laser pulse propagating through a dense plasma generates a strong quasistatic azimuthlal magnetic field. In Sec. III, we develop a test-electron model that elucidates the mechanism of direct laser acceleration of electrons assisted by the azimuthal magnetic field. In Sec. IV, we compare the results of the test-particle model with the results of PIC simulations, confirming that the model of Sec. III captures the key features of the electron dynamics. In Sec. V, we summarize our results.

II. LASER-DRIVEN MAGNETIC FIELD

In this section, we use fully relativistic kinetic three-dimensional (3D) PIC simulations to demonstrate that a high intensity laser pulse propagating through a dense plasma establishes a quasistatic configuration with a dominant azimuthal magnetic field.

The key aspect of the regime of interest is the propagation of a high-intensity laser pulse through a classically overdense plasma. In the case of a linear electromagnetic wave propagating through a cold plasma there exists an electron density cutoff, $n_e = n_c$, where n_c only depends on the wave frequency. However, the cutoff density can be increased if the electron motion in the plasma becomes relativistic. In the case of a high-intensity laser pulse, the relativistic motion is induced by the laser field itself. As a result, the cutoff frequency becomes dependent on the laser amplitude, so that a plasma with $n_e \ll a_0 n_c$ is very transparent to the laser pulse even if the plasma is classically overdense ($n_e \geqslant n_c$) [56]. This effect is often referred to as the relativistically induced transparency.

The relativistically induced transparency removes an upper limit on the electron density and opens up a possibility of driving strong currents and strong magnetic fields by a propagating laser beam. Indeed, the electron current density in a classically transparent plasma is limited by $j \approx |e| n_e v < |e| n_c c$, where v is the directed electron velocity and e is the electron charge. The limiting factor is the electron density if the laser is able to accelerate electrons to ultrarelativistic velocities. By increasing the laser amplitude a_0 (to achieve the transparency) and the plasma density, one can potentially achieve current densities approximately given by

$$j \approx \frac{n_e}{n_c} \frac{0.05}{(\lambda_0[\mu\mathrm{m}])^2}\ \mathrm{MA}/\mu\mathrm{m}^2, \tag{3}$$

where

$$\lambda_0 \equiv 2\pi c/\omega_0 \tag{4}$$

is the vacuum wavelength of the laser (ω_0 is the laser frequency) and

$$n_c = \frac{m_e \pi c^2}{\lambda_0^2 e^2} \approx \frac{1.1 \times 10^{21}\ \mathrm{cm}^{-3}}{(\lambda_0[\mu\mathrm{m}])^2} \tag{5}$$

is the corresponding critical density.

It has been confirmed using simulations that an intense laser beam indeed generates and sustains a strong azimuthal magnetic field [49,50,57] by driving a strong longitudinal current while propagating through a plasma. Additional studies have revealed that the laser propagation can become unstable in a dense relativistically transparent target [58], which makes the direction of the laser beam propagation unpredictable. The instability negatively impacts the performance of secondary sources that rely on the laser propagation, e.g., generation of gamma-ray beams [26].

One way to suppress the instability while retaining the advantages of laser propagation through a dense plasma is to use structured targets that provide optical guiding to the laser pulse. Here we consider the design where the target consists of a cylindrical channel that is filled with a material that becomes more transparent than the bulk to the laser pulse. The channel effectively serves as an optical waveguide to the laser pulse that is focused at the channel entrance. Structured targets with an initially empty channel have already been used experimentally to achieve greater control over laser interactions with solid-density targets [59–61]. Advanced target manufacturing facilities are also able to produce solid targets of variable density using the *in situ* polymerization technique [62]. The pore and thread structures are submicron, so a relatively homogeneous plasma with $n_e > 0.9 n_c$ has been achieved in experiments with high-intensity lasers [35]. It is challenging but feasible to manufacture targets with prefilled channels that we consider in our simulations [63], with the effort being justified by the improved control over laser propagation.

Figure 1 presents results of a 3D PIC simulation that illustrates three main features: laser propagation via relativistically induced transparency, generation of a strong longitudinal current, and the ability of the plasma to sustain an extreme volumetric quasistatic magnetic field. The simulation is performed using PIC code EPOCH [64]. The setup of the simulation is detailed in the Appendix.

The laser propagation through the classically overdense plasma in the channel is seen in Fig. 1(a). The peak laser

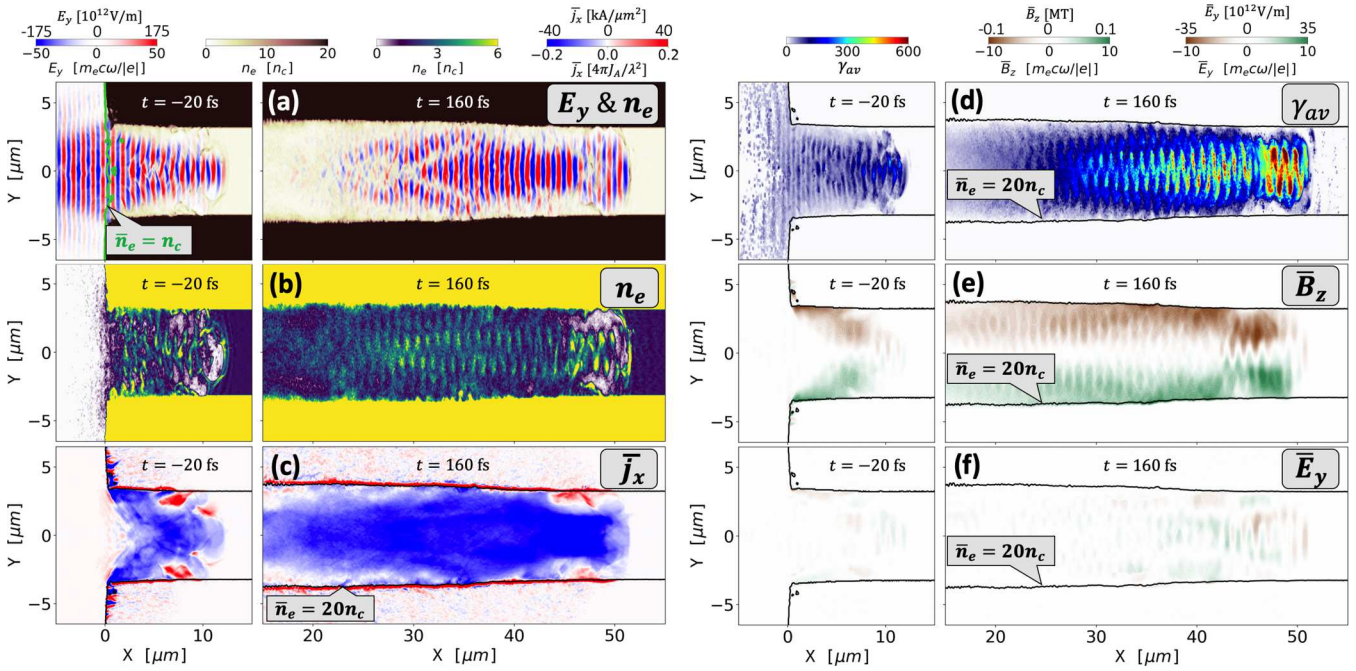

FIG. 1. 3D PIC simulation of a structured target irradiated by a high-intensity laser pulse with $a_0 = 50$. The plots are cross sections in the (x, y) plane for $z = 0$ at $t = 160$ fs and at $t = -20$ fs. (a) E_y plotted on top of the electron density n_e, with the color saturated for $n_e > 20n_c$. (b) Electron density n_e, with color saturated for $n_e > 6n_c$. (c) Time-averaged current density j_x. (d) Cell-averaged relativistic γ factor γ_{av}. (e), (f) Time-averaged magnetic and electric fields, with the overline denoting time averaging over four laser periods. $t = 0$ fs is the time when the laser reaches its peak intensity in the focal plane at $x = 0$ μm.

intensity in the absence of the target corresponds to $a_0 = 50$. Such a strong laser electric field energizes target electrons and increases the characteristic γ factor, shown in Fig. 1(d) as a cell-averaged quantity γ_{av}. This changes the optical properties of the material by increasing the effective critical density to approximately $\gamma_{av} n_c$. For our set of target and laser parameters, the channel becomes very transparent, while the bulk of the target remains opaque, creating an optical waveguide for the laser beam. As a result, the laser pulse maintains a relatively high amplitude over tens of microns, which is significantly longer than the Rayleigh range for this beam. The target structure suppresses the hosing instability that would develop in a uniform target [58]. Simulations for a uniform target with $n_e = 1.5n_c$ confirm that the laser pulse experiences a significant deviation from its original direction after propagating just tens of microns into the target.

As shown in Fig. 1(c), the channel sustains a strong laser-driven electron current density. The transverse laser electric field continuously reinjects electrons from the channel walls and keeps the channel filled with electrons for hundreds of femtoseconds, as seen in Fig. 1(b). The density in the channel remains well above $\bar{n}_e = n_c$, as evident from the position of the corresponding contour line in Fig. 1(a) that remains effectively unchanged. The overline indicates time averaging over four laser periods. The longitudinal electron current exceeds the nonrelativistic Alfvén current [65], $J_A = m_e c^3/|e| \approx$ 17 kA, by two orders of magnitude. The current density driven by the laser remains mostly uncompensated, because the return current is localized at the periphery of the laser beam [66,67]. In our case, most of the return current flows at the edge of the channel. Figure 8(a) shows the total electron current, J_0, obtained by integrating the longitudinal electron current density j_x over the area with $r < 2.5$ μm. This current exceeds $J_0 \approx 100 J_A \approx 1.7$ MA. It must be pointed out that the current limit for a beam of relativistic electrons is γJ_A [68,69], where γ is the relativistic factor associated with the directed motion. In our simulation, there are electrons with $\gamma > 100$ [see Fig. 1(d)] needed to satisfy the criterion $J_0 < \gamma J_A$.

Consistent with our expectations, the longitudinal electron current generates and sustains a strong quasistatic azimuthal magnetic field [see Fig. 1(e)]. The color in Fig. 1(e) represents $\bar{B}_z$ in the (x, y) plane at $z = 0$, where the overline again stands for time averaging. The field strength is consistent with a magnetostatic calculation that assumes a cylindrically symmetric and uniform current density, j_0, represented by a dimensionless parameter

$$\alpha \equiv \frac{\lambda_0^2}{r^2}\frac{J_0}{J_A} = \frac{\pi \lambda_0^2 j_0}{J_A}, \tag{6}$$

such that

$$B \approx 2\alpha \frac{r}{\lambda_0}\frac{m_e c^2}{|e|\lambda_0}, \tag{7}$$

where λ_0 is the vacuum wavelength of the laser. Note that B is independent of λ_0 which is simply used to make α dimensionless. It is convenient to rewrite Eq. (7) as

$$B\,[\mathrm{kT}] \approx 3.4\alpha r\,[\mu\mathrm{m}]\lambda_0^{-2}\,[\mu\mathrm{m}]. \tag{8}$$

As already stated, the total current through a cross section with $r \leqslant 2.5$ μm is $J_0 \approx 1.7$ MA. We then find from Eq. (6)

that $\alpha \approx 16$, where we set $\lambda_0 = 1\ \mu$m. Equation (8) yields $B \approx 0.14$ MT at $r = 2.5\ \mu$m, which is comparable to the result of the 3D simulation.

The laser beam also generates a transverse quasistatic electric field whose profile is shown in Fig. 1(f). The color is the amplitude normalized the same way as the amplitude of the azimuthal magnetic field. We arrive at an important conclusion, by comparing Figs. 1(e) and 1(f), that the quasistatic electric field is weak compared to the magentic field. The discussed electron injection into the channel prevents the laser beam from maintaining significant charge separation, which weakens the transverse electric field. At the same time, this is the mechanism that maintains the strong current and the resulting azimuthal magnetic field.

The configuration where the quasistatic azimuthal magnetic field is much stronger than the quasistatic transverse electric field is rather generic at high laser intensities, i.e., $a_0 \gg 1$. The ion mobility provides an additional mechanism preventing a prolonged existence of strong transverse electric fields. For example, we found that the described configuration arises even in an initially empty channel [70]. The charge of the injected electrons creates a radially inward electric field that drags ions from the channel walls, causing the channel interior to fill up. The characteristic time for this process scales as $a_0^{-1/2}$ [70]. It would take less than 50 fs for the channel to fill up and for the transverse electric field to be essentially eliminated for our laser parameters and an initially empty channel.

III. MECHANISM FOR ENHANCED ENERGY GAIN

In Sec. II, we showed that a laser pulse creates a quasistatic field configuration with a dominant azimuthal magnetic field. In what follows, we formulate a test-electron model that enables us to find the conditions for an enhanced electron energy gain from the laser pulse.

The presented simulation results demonstrate that (1) a strong current with $J_0 \gg J_A$ can be driven by the laser, (2) the current density is nearly constant inside the channel, and (3) radial plasma electric fields are much weaker than the azimuthal magnetic field sustained by the current. This motivates us to consider a homogeneous current J_0 characterized by the dimensionless parameter α defined by Eq. (6). In order to further simplify our analysis, we approximate the laser pulse by a plane electromagnetic wave with a superliminal phase velocity v_{ph}. The superluminal phase velocity is an input parameter that accounts for the presence of the plasma in the channel. It can also be used to take into account the width of the laser beam in the simulation even though we approximate it as a plane wave. Under these assumptions, the laser-driven electron acceleration in the channel can be considered as the dynamics of a test electron with a given initial transverse momentum p_i inside a prescribed combination of a plane electromagnetic wave and a static azimuthal magnetic field generated by a homogeneous current J_0. This test-electron model is illustrated in Fig. 2.

We neglect the radiation reaction [71–80] and QED effects [81–86], so that the electron dynamics is described by the

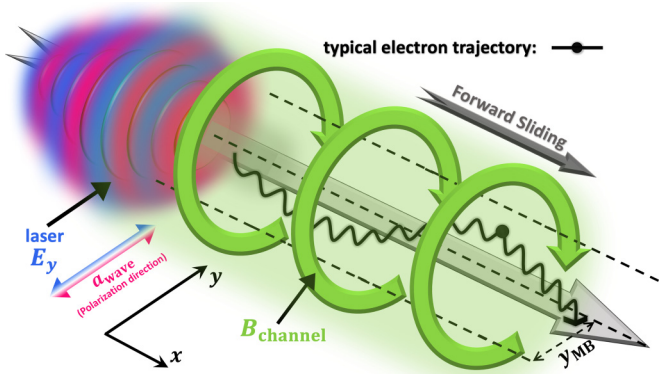

FIG. 2. Schematic diagram, where the laser propagation along x defines the forward sliding direction. The laser E field is polarized along the y axis. An electron trajectory is schematically shown with an oscillating curve.

following equations:

$$\frac{d\boldsymbol{p}}{dt} = -|e|\boldsymbol{E} - \frac{|e|}{\gamma m_e c}[\boldsymbol{p} \times \boldsymbol{B}], \tag{9}$$

$$\frac{d\boldsymbol{r}}{dt} = \frac{c}{\gamma}\frac{\boldsymbol{p}}{m_e c}, \tag{10}$$

where the electric and magnetic fields ($\boldsymbol{E}$ and $\boldsymbol{B}$) are given. Here $\gamma = \sqrt{1 + p^2/m_e^2 c^2}$ is the relativistic γ factor, $\boldsymbol{r}$ and $\boldsymbol{p}$ are the electron position and momentum, and t is the time. In the regime under consideration, $\boldsymbol{E} = \boldsymbol{E}_{\text{wave}}$ is just the laser electric field, whereas $\boldsymbol{B} = \boldsymbol{B}_{\text{wave}} + \boldsymbol{B}_{\text{channel}}$ is a superposition of the magnetic fields of the wave and the channel.

Without any loss of generality, we consider a linearly polarized wave propagating in the positive direction along the x axis with

$$\boldsymbol{E}_{\text{wave}} = \boldsymbol{e}_y E_0 \cos(\xi), \tag{11}$$

$$\boldsymbol{B}_{\text{wave}} = \boldsymbol{e}_z \frac{c}{v_{ph}} E_0 \cos(\xi), \tag{12}$$

where E_0 is the wave amplitude and

$$\xi = \omega_0 t - \omega_0 x / v_{ph} \tag{13}$$

is the phase variable. Note that the normalized wave amplitude is given by $a_0 = |e|E_0/m_e c\omega$. The magnetic field of the channel is given by

$$\boldsymbol{B}_{\text{channel}} = \frac{m_e c^2}{|e|} \nabla \times \boldsymbol{a}_{\text{channel}}, \tag{14}$$

where

$$\boldsymbol{a}_{\text{channel}} = \boldsymbol{e}_x \alpha (y^2 + z^2)/\lambda_0^2. \tag{15}$$

It can be directly verified using the equations of motion that there exists a constant of motion:

$$\gamma - \frac{v_{ph}}{c}\frac{p_x}{m_e c} + \frac{v_{ph}}{c} a_{\text{channel}} = C_1. \tag{16}$$

We are going to consider a relativistic electron that is starting its motion on axis while moving in transverse direction. We specifically set

$$p_y = -p_i, \tag{17}$$

$$p_z = 0 \tag{18}$$

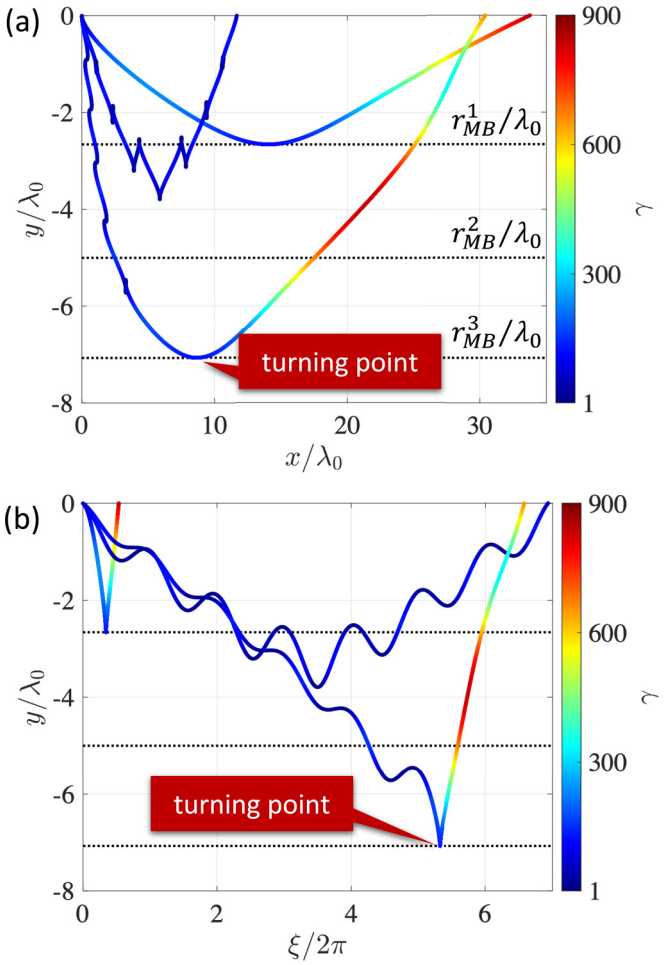

FIG. 3. Three representative electron trajectories in (x, y) space [panel (a)] and (ξ, y) space [panel (b)]. The azimuthal magnetic field corresponds to $\alpha = 1$, defined by Eq. (6). The initial values of the transverse momentum are $p_i/m_e c = 7$, 25, and 50. The dotted lines show the corresponding location of the magnetic boundary denoted as $r^{1,2,3}_{MB}$, respectively. The color along each trajectory shows the relativistic γ factor. The key laser parameters are $a_0 = 50$ and $v_{ph} = c$.

at $\xi = 0$ to mimic the electron injection observed in kinetic simulations [26]. The constant of motion for this electron is its initial γ factor γ_i:

$$C_1 = \gamma_i \equiv \sqrt{1 + p_i^2/m_e^2 c^2}. \tag{19}$$

One can use Eqs. (16) and (19) to show that the amplitude of transverse electron displacements in the channel $r \equiv \sqrt{y^2 + z^2}$ is limited by

$$r \leqslant r_{\rm MB} \equiv \frac{\lambda_0}{\sqrt{\alpha u}}[\gamma_i + (u-1)\gamma]^{1/2}, \tag{20}$$

where we introduced

$$u \equiv v_{ph}/c \tag{21}$$

for compactness. In what follows, we refer to r_{MB} as the magnetic boundary. Figure 3 shows the location of the magnetic boundary for three different values of p_i at $a_0 = 50$ and $u = v_{ph}/c = 1$.

The magnetic field of the channel causes each of the electrons to return to the axis after initially traveling outwards to the magnetic boundary. The electrons then cross the axis and move upward in the domain with $y > 0$. The trajectory at $y > 0$ has a similar pattern, with the electrons sliding in the positive direction along the x axis in the channel magnetic field that has an opposite sign. We start our analysis by focusing on the electron trajectories at $y \leqslant 0$, i.e., a single half bounce across the channel shown in Fig. 3.

A. Half bounce across the channel

One common feature of all half bounce trajectories is that they have a turning point (see Fig. 3). We mark all quantities at the turning point with a subscript $*$. By definition of the turning point, we have $p_y = 0$ (no transverse momentum) and $|y_*| = \max|y|$. It has been shown in Ref. [87] that the value of the longitudinal momentum at the turning point has a profound impact on the electron energy exchange with the laser field.

Electron energy gain from the laser pulse is closely connected to the dephasing,

$$R \equiv \frac{\gamma}{\omega_0}\frac{d\xi}{dt} = \gamma - \frac{c}{v_{ph}}\frac{p_x}{m_e c}, \tag{22}$$

that determines how quickly the electron slips with respect to the wave fronts in an instantaneous rest frame. We have $R = 1$ for an electron that is initially at rest. It is instructive to consider three limiting cases at $v_{ph} = c$ to illustrate the impact of the electron momentum on the dephasing: (1) $p_y \gg m_e c$ and $p_x = 0$; (2) $p_x < 0$, $|p_x| \gg m_e c$, and $p_y = 0$; (3) $p_x > 0$, $|p_x| \gg m_e c$, and $p_y = 0$. It follows from Eq. (22) that $R \gg 1$ in the first two cases. In contrast to that, $R \ll 1$ in the third cases correspond to an ultrarelativistic electron moving in the same direction as the laser pulse. Rapid changes in phase associated with strong dephasing prevent electrons with $p_i/m_e c = 25$ and 50 in Fig. 3 from gaining significant energy during their motion away from the axis.

The electron motion away from the axis reduces the dephasing. This can be easily shown for $v_{ph} = c$. It follows from Eq. (16) that $R = \gamma_i - a_{\rm channel} = \gamma_i - \alpha y^2/\lambda_0^2$. This relation shows that the dephasing decreases with the increase of $|y|$. We conclude that R reaches its smallest value, $R = R_*$, at the turning point, $y = y_*$. Since the electron has no transverse momentum at the turning point, the value of R_* is exclusively determined by the longitudinal momentum p_x at $y = y_*$. If p_x at the turning point is positive and relativistic, then the dephasing rate can drop well below $R = 1$. However, the dephasing remains strong if p_x is negative.

One of the key results of Ref. [87] is that the value of R_* determines the energy exchange between the electron and the laser electric field during the electron return to the axis of the channel. The energy gain from the laser increases considerably along this part of the trajectory if $R_* \ll 1$. The electron trajectories shown in Fig. 3 are in good agreement with this result. For $p_i/m_e c = 50$, we have $R_* \approx 4 \times 10^{-3}$ and the electron experiences an enhanced energy gain, returning to the axis with $\gamma \approx 654$. For $p_i/m_e c = 25$, we have $R_* \approx 11$ and the electron energy remains essentially the same. We find

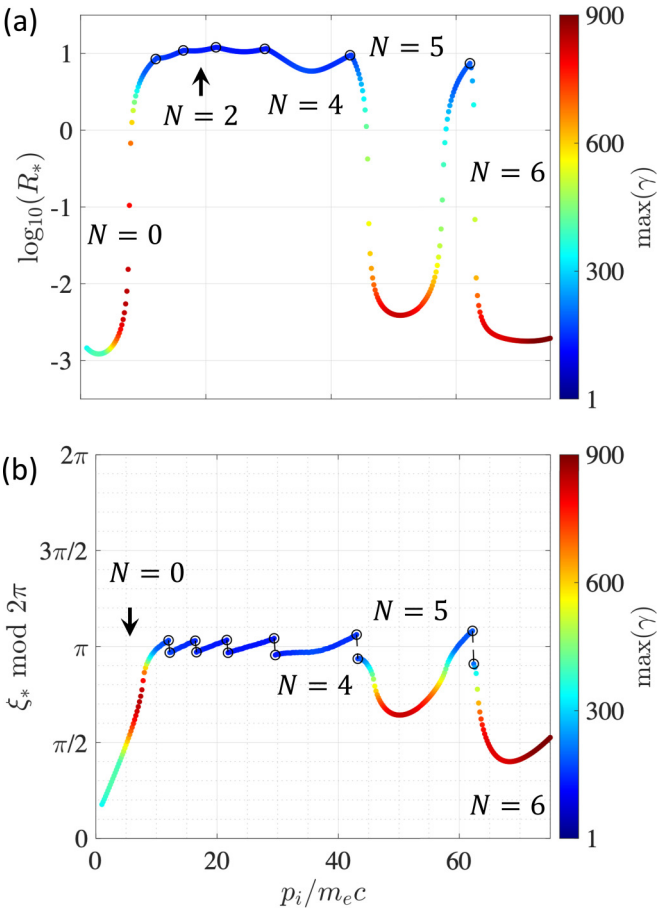

FIG. 4. Scan over transverse initial momentum p_i for a laser-irradiated electron in an azimuthal magnetic field corresponding to $\alpha = 1$ [see Eq. (6)]. (a) Electron dephasing at the turning point. (b) Laser phase at the turning point. The color in (a) and (b) is the relativistic γ factor. The laser parameters are $a_0 = 50$ and $v_{ph} = c$. The circles show boundaries of regions with different values of full oscillations N by the laser field witnessed by the electron during its motion from the axis to the turning point.

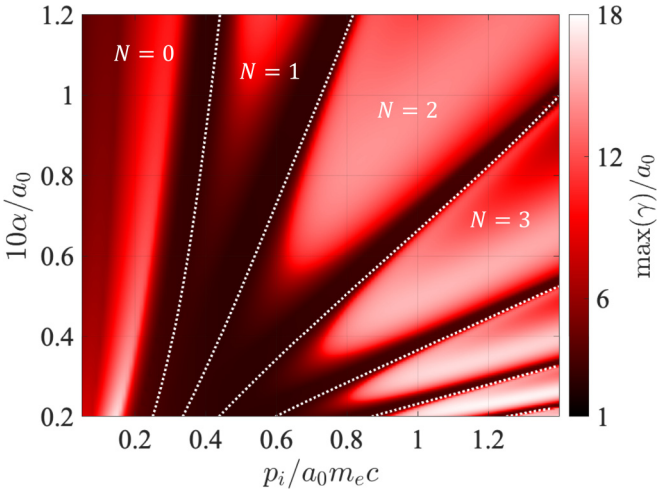

FIG. 5. Parameter scan over the initial transverse momentum p_i and normalized current density α defined by Eq. (6). The color is the maximum γ factor reached by the electron with the corresponding p_i over a single half-bounce across the channel. The dotted curves separate the regions with different values of N [see Eq. (23)], where N is the number of full oscillations by the laser field witnessed by the electron during its motion from the axis to the turning point. The scan result has been verified for $a_0 = 10$, 15, 25, 50, and 75 with $v_{ph} = c$.

that $\max(\gamma) \approx 128$ both along the trajectory prior to reaching the turning point and during the return to the axis.

In order to find a correlation between p_i and the energy gain, we have performed a parameter scan shown in Fig. 4. Figure 4(a) shows the dephasing R_* at the turning point. The color is the maximum relativistic γ factor along the entire trajectory. The figure confirms that the energy increase is connected to R_*. Figure 4(b) shows the phase of the laser field at the turning point. The electron typically reaches its turning point in a negative field. This leads to the discontinuities marked with circles. Each discontinuity corresponds to an increase of

$$N = \frac{1}{2\pi}[\xi_* - (\xi_* \bmod 2\pi)] \tag{23}$$

by one, where N is the number of full oscillations by the laser field witnessed by the electron during its motion from the axis to the turning point. In Fig. 4(a), the numbers next to each segment of the curve indicate the corresponding value of N.

In the presented scan, the electrons achieve $R_* \ll 1$ and subsequently increase their energy in two cases: (1) at low values of p_i corresponding to $N = 0$ and (2) at large values of p_i that exceed a_0m_ec. Intermediate values of p_i result in no substantial energy gain. The scan suggests that we can increase the range of p_i corresponding to the energy increase by adjusting the current density sustaining the magnetic field. By increasing α, we can reduce the time that the electron travels to the turning point, so a higher value of p_i is needed to achieve $N = 1$. This observation is confirmed by the scan over p_i and α shown in Fig. 5. For example, at $\alpha = 6$, most of the initial transverse momenta between m_ec and $70m_ec$ lead to a significant energy enhancement over the considered half bounce.

B. Similarity of solutions with different a_0

We have so far examined electron acceleration over the first half bounce across the channel for $a_0 = 50$. We have repeated the scan over p_i and α for $a_0 = 10$, 15, 25, and 75. The results look indistinguishable from the scan shown in Fig. 5. Therefore, there is a similarity between solutions with different a_0. Specifically, we find that the value of $\max(\gamma)/a_0$ remains the same for the same values of p_i/a_0m_ec and α/a_0. This is true for a scan at higher values of α shown in Fig. 7(a).

The observed similarity enables us to formulate a universal condition on the current density that ensures an energy increase for a wide range of p_i. We define a critical value of α, denoted as α_{DLA}, by the condition $10\alpha/a_0 = 1$, which yields

$$\alpha_{DLA} = a_0/10. \tag{24}$$

As seen in Fig. 5, all of the regions defined by a corresponding value of N have a significant energy increase for $\alpha > \alpha_{DLA}$.

It follows from Eq. (6) that the corresponding critical current density is

$$j_{DLA} = \frac{a_0}{10}\frac{J_A}{\pi\lambda_0^2}. \tag{25}$$

It is convenient to reformulate this condition in terms of the electron density in the plasma. The maximum current density that a plasma with a given electron density n_e can sustain is $j_e = |e|n_e c$. Using this expression in Eq. (25) for j_{DLA}, we obtain the lowest electron density that can sustain the described critical current density:

$$n_e = n_{DLA} \equiv a_0 n_c/10\pi^2 \approx 10^{-2} a_0 n_c. \tag{26}$$

The key conclusion is that n_e has to exceed n_{DLA} in order to have favorable conditions for the electron energy increase.

The determined similarity applies not only to $\max(\gamma)$, but also to the distance that the electron travels to reach this γ. Figure 7(c) shows x/λ_0 at the location where the electron reaches $\max(\gamma)$. We find that the scans for $a_0 = 10$, 15, 25, 50, and 75 are indistinguishable when plotting x/λ_0 at $\max(\gamma)$ for the same values of $p_i/a_0 m_e c$ and α/a_0. An important finding is that the distance remains independent of a_0. We can formulate this result by stating that, at $\alpha = \alpha_{DLA}$, the energy gain over a single half-bounce increases linearly with a_0 for a given $p_i/a_0 m_e c$, while the required longitudinal displacement remains the same.

C. Multiple bounces across the channel

After completing the first half bounce and returning to the axis, the electron performs a similar motion pattern at $y > 0$, i.e., another half bounce. We find that the energy gain can continue during the second half bounce for the electron that experiences an energy increase during the first half bounce. This is because the dephasing on axis is reduced due to the increase in the longitudinal momentum, as evident from Fig. 3.

Those electrons that experience no energy increase during the first half bounce can still undergo an energy gain during subsequent bounces due to differences in the laser phase and the electron momentum during the axis crossing. In order to explore this scenario, we have performed another scan where the electrons are tracked over two full bounces across the channel. The result shown in Fig. 6(a) confirms that the conditions required for the energy increase can indeed be achieved over multiple bounces even if the first half bounce shows no energy increase.

The effect of multiple bounces becomes evident when examining regions in the (p_i, α) space defined by a given N, which is the number of full laser field oscillations to the turning point during the first half bounce. These regions are shown in Fig. 6(a) using the dotted curves that match those shown in Fig. 5. We observe that the areas with the increased energy expand within each region. However, each region remains well defined by a visible reduction in $\max(\gamma)$ at its boundary. This feature is responsible for the low energy at $10\alpha/a_0 = 0.2$ in the regions with $N = 1$, 2, and 3 even after two full bounces.

The electrons travel along the axis of the channel while performing the transverse bounces. The traveled distance

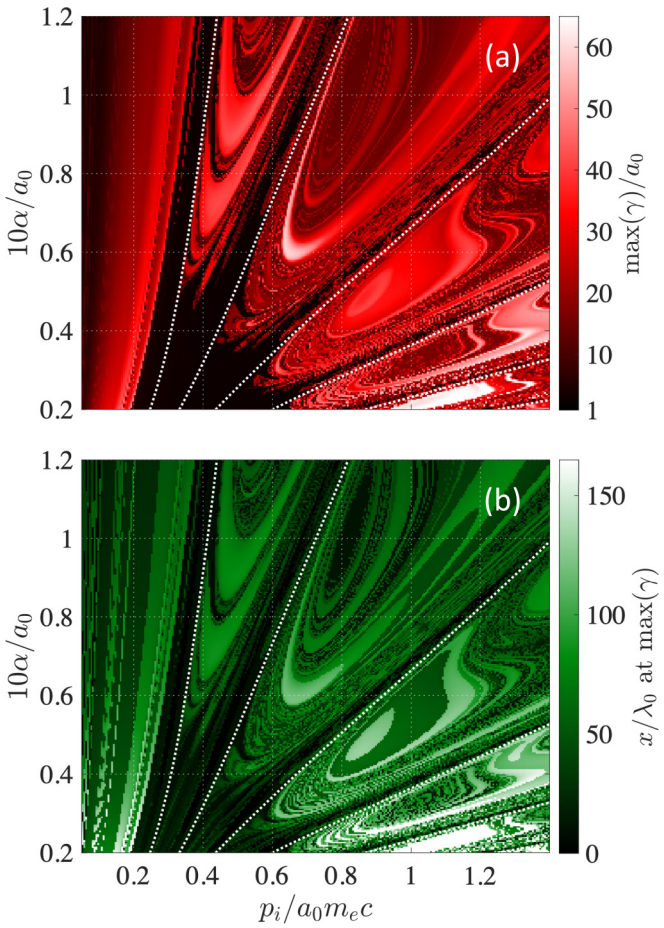

FIG. 6. Parameter scan over the initial transverse momentum p_i and normalized current density α defined by Eq. (6). (a) Maximum γ factor reached by an electron over two full bounces across the channel. (b) The location where the electron reaches its maximum γ. The dotted curves are the same as in Fig. 5 to aid the comparison. The laser parameters are $a_0 = 50$ and $v_{ph} = c$.

increases with each bounce, so it might be impractical to rely on having many bounces to achieve a significant energy gain. As shown in Fig. 6(b), even two bounces can require a longitudinal displacement exceeding $100\lambda_0$. We thus limit our consideration to just two bounces across the channel. One important observation that follows from Fig. 6(b) is that the longitudinal travel distance decreases with the increase of α. The underlying reason is that an electron with the same p_i samples a stronger magnetic field at higher α, which reduces the radius of curvature of the electron trajectory and makes the distance associated with each half bounce shorter [88].

The energy gain becomes more effective with the increase of α. Figure 7(a) shows a scan for $1 \leqslant 10\alpha/a_0 \leqslant 4$, where the electron is tracked over the first half bounce. At such a high current density, the electron at most experiences two full oscillations of the laser pulse for $p_i < a_0 m_e c$. Most of the parameter space shown in the plots corresponds to considerable energy gain, which agrees with the conclusion at the end of Sec. III A. This energy gain is achieved over a relatively short distance, as evident from Fig. 7(c). This is another advantage of having a high current density, i.e., large α.

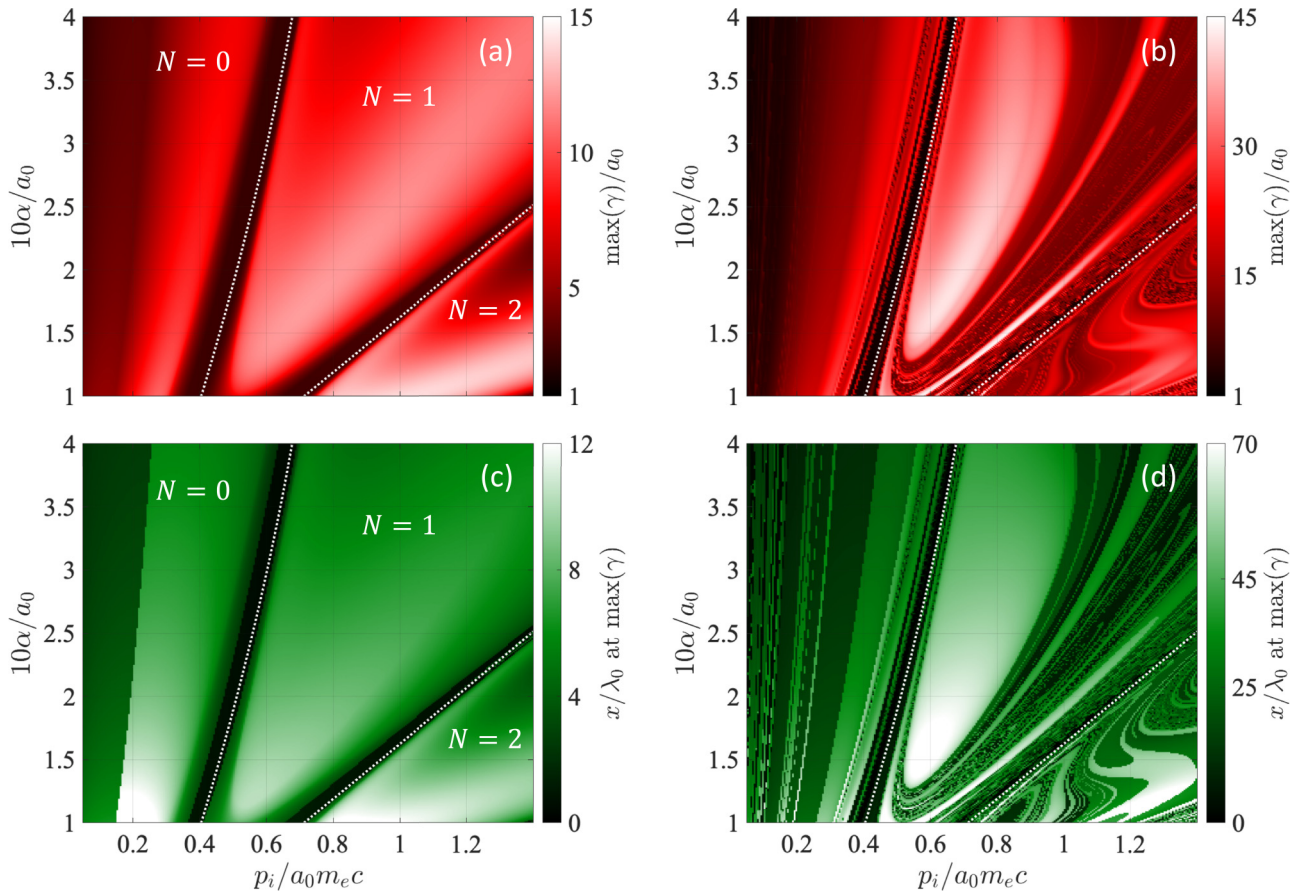

FIG. 7. Two scans over the initial transverse momentum p_i and normalized current density α: (a) and (c) are for one half bounce; (b) and (d) are for two bounces. Panels (a) and (b) are the maximum γ achieved by an electron. Panels (c) and (d) are the corresponding location. The dotted curves in (a) and (c) separate the regions with different values of N [see Eq. (23)], where N is the number of full oscillations by the laser field witnessed by the electron during its motion from the axis to the turning point. The dotted curves in (b) and (d) are the same as in (a) and (c) to aid the comparison between the two scans. The laser parameters are $a_0 = 50$ and $v_{ph} = c$. Panels (a) and (c) also represent scans for $a_0 = 10$, 15, 25, and 75 with $v_{ph} = c$.

The energy gain for this range of α also increases over multiple bounces across the channel. The result of a scan for two bounces is shown in Fig. 7(b). The typical maximum γ is only slightly reduced compared to the scan shown in Fig. 6(a) ($0.2 \leqslant 10\alpha/a_0 \leqslant 1.2$). However, the distance traveled by the electron to reach the maximum γ is reduced considerably [compare Figs. 7(d) and 6(b)]. For example, at $a_0 = 50$, an electron with $p_i = 40 m_e c$ reaches $\max(\gamma) \approx 1800$ already at $x \approx 51\lambda_0$ in a magnetic field corresponding to $\alpha = 15$.

Based on the presented scans, we conclude that a strong static azimuthal magnetic field can facilitate a rapid energy transfer from the laser pulse to an accelerated electron via transverse deflections.

IV. ENERGY GAIN IN PIC SIMULATIONS

It is shown in Sec. III using a test-electron model that a strong azimuthal magnetic field sustained by a uniform longitudinal current density can assist direct laser acceleration of electrons. In what follows, we examine results of PIC simulations and compare them to the predictions of the model from Sec. III.

We start by revisiting the 3D simulation discussed in Sec. II. In this simulation, an intense laser beam creates a magnetic field configuration similar to that used in the test-electron model. The current J_0 obtained by integrating the longitudinal current density over a cylinder whose radius is 2.5 μm is shown in Fig. 8(a). According to Eq. (6), $\alpha = 15$ corresponds to $|J_0| \approx 94 J_A$. We can then use this value of α to make a comparison with the scans performed for the test-electron model.

In the simulation, the peak laser amplitude (without the target) is $a_0 = 50$. It follows from Eq. (24) that $\alpha_{DLA} = 5$ for this a_0. The value of $\alpha = 15$ that we observe in the simulation exceeds α_{DLA}, so we should expect a significant energy gain for most of the electrons injected into the channel, i.e., $\max(\gamma)$ between 1000 and 2000 based on Fig. 7(b). The distance that the electron would need to travel along the channel to reach these values of γ is roughly $60\lambda_0$ [see Fig. 7(d)]. We use Eq. (20) to estimate that the magnetic boundary for the electrons with $p_i \leqslant 94 m_e c$ is located inside the considered cylinder with radius of 2.5 μm. For simplicity, we neglect the boundary widening due to the superluminosity by setting $u = 1$ in Eq. (20). The aspect of widening is addressed later

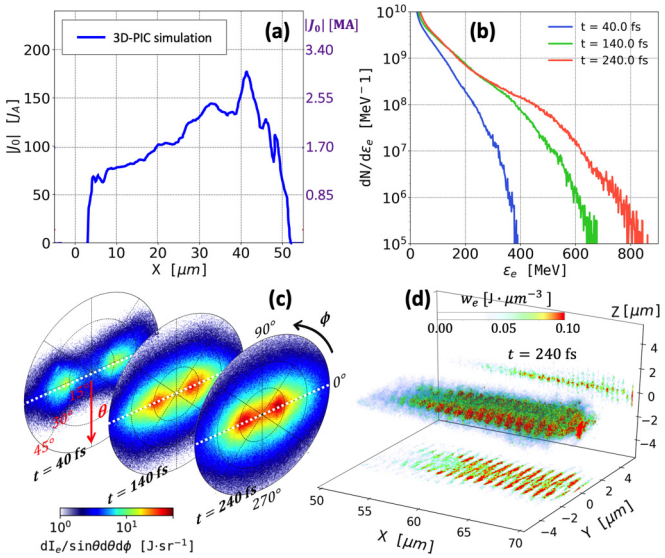

FIG. 8. Results of a 3D PIC simulation: (a) laser driven current, (b) electron energy spectra, and (c) angular and (d) spatial distributions of energetic electrons. The total current J_0 is the integral of j_x over an area with $r < 2.5$ μm at $t = 160$ fs. Panel (c) shows the electron energy dI_e associated with a solid angle in momentum space (a detailed description is given in the text). Panel (d) shows the electron energy density w_e.

in this section once the phase velocity is determined from the simulations.

Figure 8 shows three snapshots of the electron energy spectrum in the considered 3D PIC simulation. In good agreement with the test-electron model, the electron energies are increasing over time. Here $t = 0$ fs is the time when the laser reaches its peak intensity in the focal plane located at the channel entrance. The cutoff energy reaches 800 MeV at $t =$ 240 fs, which corresponds to $\gamma \approx 1570$. This value is within the range predicted by the test-electron model. A snapshot of the electron energy density w_e at $t = 240$ fs is shown in Fig. 8(d). Most of the energetic electrons are concentrated between 55 and 70 μm. This scale again agrees with the prediction of the test-electron model (most of the electrons are injected near the channel opening). The important point here is that an extended propagation distance is not required to achieve $\gamma \approx 1500$.

One of the assumptions in our model is that the electron trajectory remains flat. The 3D simulation allows us to examine and confirm the validity of this assumption. Figure 8(c) represents an angular distribution of energetic electrons in momentum space (p_x, p_y, p_z), where $\phi = \arctan(p_z/p_y)$ is the azimuthal angle and $\theta = \arctan\left[(p_y^2 + p_z^2)^{1/2}/p_x\right]$ is the polar angle. In order to aid the visualization, we have plotted $dI_e/d\Omega$, where dI_e is the electron energy associated with a solid angle $d\Omega = \sin\theta\, d\theta\, d\phi$ in momentum space. The momentum of an electron oscillating in the (x, y) plane at $z = 0$ is shown with a white dotted line. For all three snapshots in Fig. 8(c), most of the energy is concentrated near this line. These snapshots correspond to the energy spectra shown in Fig. 8(b). We can thus conclude that the laser-accelerated electrons indeed tend to move along flat trajectories.

The localization of energetic electrons in the (x, y) plane is further confirmed by the snapshot of the electron energy density w_e shown in Fig. 8(d). It is worth emphasizing that this is the polarization plane of the laser electric field. The transverse displacement of the energetic electrons in this plane is constrained to $|y| < 2$ μm, which is smaller than the channel radius, $R = 3.2$ μm. This confirms the transverse electron confinement by the azimuthal magnetic field in the region with a nearly uniform current density.

In order to obtain further details regarding the electron acceleration process, we perform particle tracking. Frequent data outputs for the electric field components, electron momenta, and electron locations are required. We achieve the desired time resolution by tracking the electrons in a 2D simulation with a setup similar to that used for the 3D simulation. The setup of the simulation is detailed in the Appendix. The 3D simulation has confirmed that the energetic electrons roughly stay in the (x, y) plane. That is why the 2D simulation with a laser electric field polarized in the plane of the simulation is a qualitatively reasonable approximation in terms of capturing the key physics, while it is also affordable in terms of postprocessing.

We have analyzed 5% of the electrons that are randomly picked from the tail of the electron energy distribution ($\varepsilon_e >$ 650 MeV) at $t = 200$ fs and we have found that the energy enhancement process and the electron trajectories have key similarities to the regime described by the test-electron model. For example, trajectories of 20 tracked electrons are shown in Fig. 9(f). The dotted black lines mark the boundary of the bulk material. We find that the electrons are injected into the channel from its periphery close to the channel entrance. The electrons are being clearly confined in the transverse direction by the azimuthal magnetic field as they move along the channel and gain energy (the color indicates their γ factor). Indeed, their transverse displacement, $|y| < 1.6$ μm, is significantly less than the transverse size of the channel, $|y| < 3.2$ μm.

The details of the acceleration process are shown in Figs. 9(a)–9(e) for a single electron from the tracked population. It is evident from the time evolution of the work done by transverse and longitudinal electric fields [W_y and W_x in Fig. 9(a)] that the electron energy is predominantly contributed by the transverse laser electric field E_y. Electron oscillations with respect to this field are shown in Fig. 9(c), where the background color is the instantaneous electric field E_y exerted on the electron. The azimuthal magnetic field changes the orientation of the transverse electron velocity and allows the velocity to remain antiparallel to E_y over extended segments of the electron trajectory (marked using the green outline). The electron gains energy while moving along these segments, as shown in Fig. 9(b) where the plotted quantity is $dW_y/dt = -(p_y/\gamma)E_y$. In agreement with our model, the electron energy is accumulated over multiple oscillations in the laser pulse. The trajectory of the considered electron in momentum space is shown in Fig. 9(e).

Figure 9(d) shows the electron trajectory relative to the wave fronts of the laser pulse in a window moving along the axis of the channel with the speed of light. Specifically, we define the coordinate in the moving window as $\Delta = x - ct$, whereas the background color is $E_y(y = 0)$, which is the

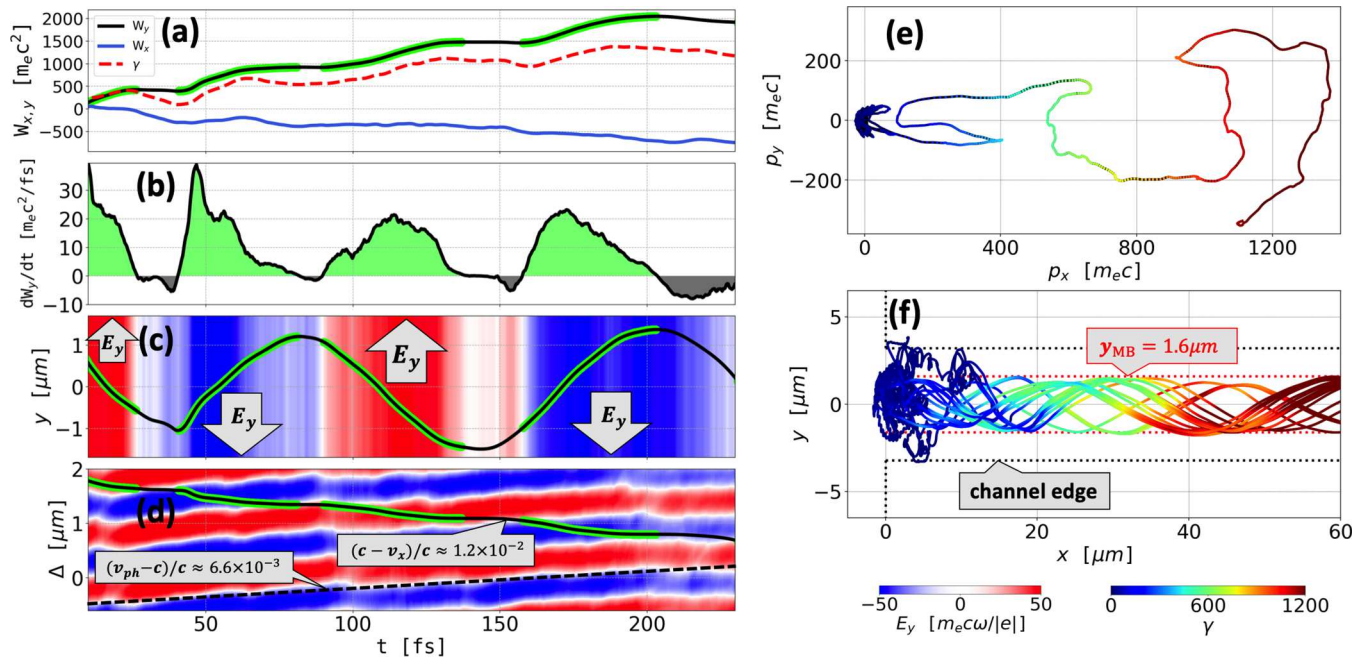

FIG. 9. Particle tracking from the 2D PIC simulation. (a) Work by transverse and longitudinal electric fields. (b) The rate of the energy transfer by E_y to the accelerated electron. (c) Transverse oscillations with respect to the wave fronts of E_y. (d) Electron trajectory in a window moving with the speed of light. The background color is E_y at $y = 0$ and the vertical coordinate is $\Delta = x - ct$. (e) Electron trajectory in the momentum space (p_x, p_y). (f) Trajectories for 20 electrons whose energy exceeds 650 MeV at $t = 200$ fs. Note that the thick part of the curves in panels (a)–(d) (highlighted with green) indicates the part of the trajectory where the electron is gaining energy from E_y.

transverse laser electric field at the central axis. The moving window makes it easy to distinguish between superluminal and subluminal velocities. As one would expect, the wave fronts have a positive slope, representing a superluminal phase velocity v_{ph}. We find that $v_{ph} - c \approx 6.6 \times 10^{-3}c$. This result quantifies the impact of the relativistically induced transparency on the laser propagation through the channel whose electron density is above n_c. The trajectory of the accelerated electron has a negative slope because the accelerated electron is moving slower than the speed of light. We find that $c - v_x \approx 1.2 \times 10^{-2}c$. In this case, the dephasing between the electron and the wave fronts is primarily influenced by v_x rather than by v_{ph}, since $c - v_x > v_{ph} - c$ [39]. One can then simplify the analysis of the electron dynamics by setting $v_{ph} \approx c$, as is done in the parameter scans presented in Sec. III. Additional parameter scans with $u - 1 = (v_{ph} - c)/c \approx 6.6 \times 10^{-3}$ yield results that are similar to those shown in Fig. 7, which further supports the presented argument.

To conclude this section, we use the obtained phase velocity to assess the electron trajectory widening during the observed energy increase. According to the expression for the location of the magnetic boundary given by Eq. (20), the trajectory widening becomes appreciable only after $(u - 1)\gamma$ becomes comparable to γ_i. Taking into account that the observed cutoff is at $\gamma \approx 1500$ [see Fig. 8(b)], we conclude that the trajectory widening is relatively unimportant for $\gamma_i > 10$. At $\gamma_i \leqslant 10$, the widening must be considered, but the electron energy gain is greatly suppressed [e.g., see Fig. 7(b)]. Moreover, even if an electron with $\gamma_i = 10$ manages to achieve $\gamma \approx 1500$, the location of the magnetic boundary would only increase from 0.82 μm to 1.15 μm. The conclusions of our analysis strongly depend on the radius of the channel and on the level of the relativistically induced transparency. Both of these aspects influence the value of $u - 1$ and their impact on the electron dynamics must be checked for a given setup.

V. SUMMARY

We have identified and characterized a mechanism of direct laser acceleration assisted by a strong laser-driven azimuthal magnetic field. We have demonstrated using kinetic simulations of a laser-irradiated structured target with a relativistically transparent channel that (1) a strong current with $J_0 \gg J_A$ can be driven by the laser, (2) the current density is nearly constant inside the channel, and (3) radial plasma electric fields are much weaker than the azimuthal magnetic field sustained by the current. We used these observations to formulate a test-electron model. The key result of the model is a significant energy increase over a relatively short displacement along the laser propagation. We found a similarity between solutions with different a_0: the value of $\max(\gamma)/a_0$ remains the same for the same values of $p_i/a_0 m_e c$ and α/a_0. The observed similarity enabled us to formulate a universal condition on the current density that ensures an energy increase for a wide range of initial momenta:

$$j_{DLA} = \frac{a_0}{10}\frac{J_A}{\pi\lambda_0^2}. \tag{27}$$

The lowest electron density that can sustain the described critical current density is

$$n_e = n_{DLA} \equiv a_0 n_c/10\pi^2 \approx 10^{-2} a_0 n_c. \tag{28}$$

The key conclusion is that n_e has to exceed n_{DLA} in order to have favorable conditions for the electron energy increase. We have confirmed the key features of the model using 3D and 2D PIC simulations.

One advantage of the described regime is that it relies on laser interaction with a large number of electrons. The electron density in the channel is $1.5n_c$ in the presented 3D PIC simulation. As a result, the considered 160 fs laser pulse can generate 2.2 nC of electrons whose energies exceed 400 MeV. This indicates that the electron acceleration assisted by the plasma magnetic field mechanism can facilitate gamma-ray emission [19–21,23,24,26,27,29,89].

Another important distinction of the discussed acceleration regime is that it requires a relatively short propagation distance by the electrons along the axis of the channel. For example, at the critical current density j_{DLA}, the energy gain over a single half-bounce across the channel increases linearly with a_0 for a given $p_i/a_0 m_e c$, while the required longitudinal displacement remarkably remains the same. This trend can be advantageous when implementing this regime at the next generation laser facilities, such as ELI [46], Apollon [47], and XCELS [48], that are expected to achieve unprecedented laser intensities [86]. Furthermore, the radiation reaction that will become important at these intensities can be beneficial in the considered setup even though it is an energy loss mechanism [90].

ACKNOWLEDGMENTS

The work has been supported by the National Science Foundation (Grant No. 1821944), the National Basic Research Program of China (Grant No. 2013CBA01502), and NSFC (Grant No. 11535001). Simulations were performed by EPOCH (developed under UK EPSRC Grants No. EP/G054950/1, No. EP/G055165/1, and No. EP/G056803/1) using HPC resources provided by TACC at the University of Texas. This work also used the Extreme Science and Engineering Discovery Environment (XSEDE) through allocation TG-PHY190034, supported by NSF Grant No. ACI-1548562.

APPENDIX: PARTICLE-IN-CELL SIMULATION SETUP

All of the simulations in the paper were performed using PIC code EPOCH [64]. In our 3D PIC simulation, a laser pulse irradiates a uniform target with a prefilled cylindrical channel. The central axis of the laser pulse is aligned with the central axis of the channel that is also the x axis of the Cartesian system of coordinates used in our simulation [see Fig. 1(a)]. The laser pulse is incident from the left and it is focused at the channel entrance located at $x = 0$ μm.

In the absence of the target, the laser pulse has a Gaussian focal spot of 4.7 μm (full width at half maximum for the laser intensity), with a peak intensity of 3.4×10^{21} W/cm^2 and a normalized laser amplitude of $a_0 \approx 50$. It is linearly polarized with a wavelength of $\lambda_0 = 1$ μm. The laser electric field in the focal plane is directed along the y axis, while the magnetic field is directed along the z axis. The time profile of the electric field at $x = y = z = 0$ μm is $|E_y| = E_0 \cos(\pi t/\tau)$ for $|t| < \tau/2$ and it is $|E_y| = 0$ for $|t| > \tau/2$, where E_0 is the maximum field amplitude, $\tau = 160$ fs is the pulse duration, and $t = 0$ fs is the time when the laser reaches its peak intensity in the focal plane. We choose this time profile in order to make our 3D simulation computationally affordable. The important physics takes place inside the laser pulse, so the laser pulse duration is more important in the context of our problem than the rise time.

The target is initialized as fully ionized carbon, which is a good approximation for plastic targets. The electron density in the bulk is set at $n_e = 25n_c$, where n_c is the critical density that determines the electron density cutoff for linear electromagnetic waves with $\lambda_0 = 1$ μm. The target has a cylindrical channel with radius $R = 3.2$ μm. The initial electron density inside the channel is set at $n_e = 1.5n_c$, so that it is opaque at laser amplitudes below 10^{18} W/cm^2. We represent electrons by 20 macroparticles per cell, while the ions are represented by 10 macroparticles per cell. No ionization takes place during our simulation, which significantly reduces computational costs. This approach is justified by performing additional simulations with field ionization. These simulations show that the leading edge of the considered laser pulse can fully ionize carbon well before the intensity reaches its peak value.

In order to achieve a significant electron energy gain in our simulation, we use a target that is 75 μm long. The electrons are accelerated as they move forward with the laser pulse, which is the reason why an extended target is required. The size of our simulation domain in the (x, y, z) space is 80 μm $\times$ 24 μm $\times$ 24 μm and the cell size is $(1/20)$ μm $\times$ $(1/15)$ μm $\times$ $(1/15)$ μm.

A well-resolved particle tracking procedure requires frequent outputs of particle data and electric field components. We achieve this by performing a 2D simulation with a setup similar to that used in 3D. In the (x, y) space, the domain has the same size, but the cell size is smaller [$(1/50)$ μm $\times$ $(1/30)$ μm]. We use 40 macroparticles per cell for the electrons and 20 macroparticles per cell for ions. To track the electron dynamics, we output the simulation data ten times per laser period. The electrons are tracked over 400 fs. We have repeated the 2D simulation after doubling the spatial resolution. The energetic part of the resulting electron spectrum has remained unchanged, which confirms that our results are not sensitive to the resolution used for electron tracking.

[1] D. Strickland and G. Mourou, Opt. Commun. **55**, 447 (1985).
[2] G. A. Mourou, T. Tajima, and S. V. Bulanov, Rev. Mod. Phys. **78**, 309 (2006).
[3] E. Esarey, C. B. Schroeder, and W. P. Leemans, Rev. Mod. Phys. **81**, 1229 (2009).
[4] H. Daido, M. Nishiuchi, and A. S. Pirozhkov, Rep. Prog. Phys. **75**, 056401 (2012).
[5] A. Macchi, M. Borghesi, and M. Passoni, Rev. Mod. Phys. **85**, 751 (2013).
[6] F. Mackenroth, A. Gonoskov, and M. Marklund, Phys. Rev. Lett. **117**, 104801 (2016).

[7] H. Chen, S. C. Wilks, J. D. Bonlie, E. P. Liang, J. Myatt, D. F. Price, D. D. Meyerhofer, and P. Beiersdorfer, Phys. Rev. Lett. **102**, 105001 (2009).

[8] H. Chen, S. C. Wilks, D. D. Meyerhofer, J. Bonlie, C. D. Chen, S. N. Chen, C. Courtois, L. Elberson, G. Gregori, W. Kruer, O. Landoas, J. Mithen, J. Myatt, C. D. Murphy, P. Nilson, D. Price, M. Schneider, R. Shepherd, C. Stoeckl, M. Tabak *et al.*, Phys. Rev. Lett. **105**, 015003 (2010).

[9] H. Chen, F. Fiuza, A. Link, A. Hazi, M. Hill, D. Hoarty, S. James, S. Kerr, D. D. Meyerhofer, J. Myatt, J. Park, Y. Sentoku, and G. J. Williams, Phys. Rev. Lett. **114**, 215001 (2015).

[10] G. Sarri, K. Poder, J. Cole, W. Schumaker, A. Di Piazza, B. Reville, T. Dzelzainis, D. Doria, L. Gizzi, G. Grittani *et al.*, Nat. Commun. **6**, 6747 (2015).

[11] I. Pomerantz, E. McCary, A. R. Meadows, A. Arefiev, A. C. Bernstein, C. Chester, J. Cortez, M. E. Donovan, G. Dyer, E. W. Gaul, D. Hamilton, D. Kuk, A. C. Lestrade, C. Wang, T. Ditmire, and B. M. Hegelich, Phys. Rev. Lett. **113**, 184801 (2014).

[12] S. Corde, K. Ta Phuoc, G. Lambert, R. Fitour, V. Malka, A. Rousse, A. Beck, and E. Lefebvre, Rev. Mod. Phys. **85**, 1 (2013).

[13] F. Albert and A. G. R. Thomas, Plasma Phys. Controlled Fusion **58**, 103001 (2016).

[14] T. Tajima and J. M. Dawson, Phys. Rev. Lett. **43**, 267 (1979).

[15] W. P. Leemans, A. J. Gonsalves, H. S. Mao, K. Nakamura, C. Benedetti, C. B. Schroeder, C. Tóth, J. Daniels, D. E. Mittelberger, S. S. Bulanov, J. L. Vay, C. G. R. Geddes, and E. Esarey, Phys. Rev. Lett. **113**, 245002 (2014).

[16] A. J. Gonsalves, K. Nakamura, J. Daniels, C. Benedetti, C. Pieronek, T. C. H. de Raadt, S. Steinke, J. H. Bin, S. S. Bulanov, J. van Tilborg, C. G. R. Geddes, C. B. Schroeder, C. Toth, E. Esarey, K. Swanson, L. Fan-Chiang, G. Bagdasarov, N. Bobrova, V. Gasilov, G. Korn *et al.*, Phys. Rev. Lett. **122**, 084801 (2019).

[17] A. Pukhov, Z.-M. Sheng, and J. Meyer-ter-Vehn, Phys. Plasmas **6**, 2847 (1999).

[18] A. Arefiev, V. Khudik, A. Robinson, G. Shvets, L. Willingale, and M. Schollmeier, Phys. Plasmas **23**, 056704 (2016).

[19] T. Nakamura, J. K. Koga, T. Z. Esirkepov, M. Kando, G. Korn, and S. V. Bulanov, Phys. Rev. Lett. **108**, 195001 (2012).

[20] C. P. Ridgers, C. S. Brady, R. Duclous, J. G. Kirk, K. Bennett, T. D. Arber, A. P. L. Robinson, and A. R. Bell, Phys. Rev. Lett. **108**, 165006 (2012).

[21] C. S. Brady, C. P. Ridgers, T. D. Arber, A. R. Bell, and J. G. Kirk, Phys. Rev. Lett. **109**, 245006 (2012).

[22] C. Ridgers, C. Brady, R. Duclous, J. Kirk, K. Bennett, T. Arber, and A. Bell, Phys. Plasmas **20**, 056701 (2013).

[23] L. L. Ji, A. Pukhov, I. Y. Kostyukov, B. F. Shen, and K. Akli, Phys. Rev. Lett. **112**, 145003 (2014).

[24] L. Ji, A. Pukhov, E. Nerush, I. Y. Kostyukov, B. Shen, and K. Akli, Phys. Plasmas **21**, 023109 (2014).

[25] X.-L. Zhu, Y. Yin, T.-P. Yu, F.-Q. Shao, Z.-Y. Ge, W.-Q. Wang, and J.-J. Liu, New J. Phys. **17**, 053039 (2015).

[26] D. J. Stark, T. Toncian, and A. V. Arefiev, Phys. Rev. Lett. **116**, 185003 (2016).

[27] T. W. Huang, A. P. L. Robinson, C. T. Zhou, B. Qiao, B. Liu, S. C. Ruan, X. T. He, and P. A. Norreys, Phys. Rev. E **93**, 063203 (2016).

[28] B. Qiao, H. Chang, Y. Xie, Z. Xu, and X. He, Phys. Plasmas **24**, 123101 (2017).

[29] Z. Gong, R. H. Hu, H. Y. Lu, J. Q. Yu, D. H. Wang, E. G. Fu, C. E. Chen, X. T. He, and X. Q. Yan, Plasma Phys. Controlled Fusion **60**, 044004 (2018).

[30] Y.-J. Gu, O. Klimo, S. V. Bulanov, and S. Weber, Commun. Phys. **1**, 93 (2018).

[31] T. Huang, C. M. Kim, C. Zhou, M. H. Cho, K. Nakajima, C. M. Ryu, S. Ruan, and C. H. Nam, New J. Phys. **21**, 013008 (2019).

[32] E. C. Schreiber, R. S. Canon, B. T. Crowley, C. R. Howell, J. H. Kelley, V. N. Litvinenko, S. O. Nelson, S. H. Park, I. V. Pinayev, R. M. Prior, K. Sabourov, M. Spraker, W. Tornow, Y. Wu, E. A. Wulf, and H. R. Weller, Phys. Rev. C **61**, 061604(R) (2000).

[33] E. Kwan, G. Rusev, A. S. Adekola, F. Donau, S. L. Hammond, C. R. Howell, H. J. Karwowski, J. H. Kelley, R. S. Pedroni, R. Raut, A. P. Tonchev, and W. Tornow, Phys. Rev. C **83**, 041601(R) (2011).

[34] B. Liu, H. Y. Wang, J. Liu, L. B. Fu, Y. J. Xu, X. Q. Yan, and X. T. He, Phys. Rev. Lett. **110**, 045002 (2013).

[35] L. Willingale, A. V. Arefiev, G. J. Williams, H. Chen, F. Dollar, A. U. Hazi, A. Maksimchuk, M. J.-E. Manuel, E. Marley, W. Nazarov, T. Z. Zhao, and C. Zulick, New J. Phys. **20**, 093024 (2018).

[36] S. Palaniyappan, B. M. Hegelich, H.-C. Wu, D. Jung, D. C. Gautier, L. Yin, B. J. Albright, R. P. Johnson, T. Shimada, S. Letzring *et al.*, Nat. Phys. **8**, 763 (2012).

[37] J. C. Fernández, D. Cort Gautier, C. Huang, S. Palaniyappan, B. J. Albright, W. Bang, G. Dyer, A. Favalli, J. F. Hunter, J. Mendez *et al.*, Phys. Plasmas **24**, 056702 (2017).

[38] A. Arefiev, A. Robinson, and V. Khudik, J. Plasma Phys. **81**, 475810404 (2015).

[39] A. Robinson, A. Arefiev, and V. Khudik, Phys. Plasmas **22**, 083114 (2015).

[40] A. P. L. Robinson, A. V. Arefiev, and D. Neely, Phys. Rev. Lett. **111**, 065002 (2013).

[41] S. C. Wilks, W. L. Kruer, M. Tabak, and A. B. Langdon, Phys. Rev. Lett. **69**, 1383 (1992).

[42] C. Gahn, G. D. Tsakiris, A. Pukhov, J. Meyer-ter-Vehn, G. Pretzler, P. Thirolf, D. Habs, and K. J. Witte, Phys. Rev. Lett. **83**, 4772 (1999).

[43] B. Walton, S. Mangles, Z. Najmudin, M. Tatarakis, M. Wei, A. Gopal, C. Marle, A. Dangor, K. Krushelnick, S. Fritzler *et al.*, Phys. Plasmas **13**, 113103 (2006).

[44] S. Kneip, S. R. Nagel, C. Bellei, N. Bourgeois, A. E. Dangor, A. Gopal, R. Heathcote, S. P. D. Mangles, J. R. Marques, A. Maksimchuk, P. M. Nilson, K. T. Phuoc, S. Reed, M. Tzoufras, F. S. Tsung, L. Willingale, W. B. Mori, A. Rousse, K. Krushelnick, and Z. Najmudin, Phys. Rev. Lett. **100**, 105006 (2008).

[45] V. Khudik, A. Arefiev, X. Zhang, and G. Shvets, Phys. Plasmas **23**, 103108 (2016).

[46] Extreme light infrastructure project, www.eli-laser.eu

[47] J. Zou, C. Le Blanc, D. Papadopoulos, G. Chériaux, P. Georges, G. Mennerat, F. Druon, L. Lecherbourg, A. Pellegrina, and P. Ramirez, High Power Laser Sci. Eng. **3**, e2 (2015).

[48] Exawatt center for extreme light studies, www.xcels.iapras.ru

[49] A. Pukhov and J. Meyer-ter-Vehn, Phys. Rev. Lett. **76**, 3975 (1996).

[50] B. F. Lasinski, A. B. Langdon, S. P. Hatchett, M. H. Key, and M. Tabak, Phys. Plasmas **6**, 2041 (1999).

[51] S. Bulanov, D. Dylov, T. Z. Esirkepov, F. Kamenets, and D. Sokolov, Plasma Phys. Rep. **31**, 369 (2005).

[52] T. Nakamura, S. V. Bulanov, T. Z. Esirkepov, and M. Kando, Phys. Rev. Lett. **105**, 135002 (2010).

[53] S. S. Bulanov, V. Y. Bychenkov, V. Chvykov, G. Kalinchenko, D. W. Litzenberg, T. Matsuoka, A. G. Thomas, L. Willingale, V. Yanovsky, K. Krushelnick *et al.*, Phys. Plasmas **17**, 043105 (2010).

[54] O. Jansen, T. Wang, D. Stark, E. d'Humières, T. Toncian, and A. Arefiev, Plasma Phys. Controlled Fusion **60**, 054006 (2018).

[55] T. Wang, X. Ribeyre, Z. Gong, O. Jansen, E. d'Humières, D. Stutman, T. Toncian, and A. Arefiev, Phys. Rev. Applied **13**, 054024 (2020).

[56] P. Gibbon, *Short Pulse Laser Interactions with Matter* (World Scientific Publishing Company, Singapore, 2004).

[57] T. Wang, T. Toncian, M. S. Wei, and A. V. Arefiev, Phys. Plasmas **26**, 013105 (2019).

[58] T. W. Huang, C. T. Zhou, H. Zhang, S. Z. Wu, B. Qiao, X. T. He, and S. C. Ruan, Phys. Rev. E **95**, 043207 (2017).

[59] J. Snyder, L. L. Ji, K. M. George, C. Willis, G. E. Cochran, R. L. Daskalova, A. Handler, T. Rubin, P. L. Poole, D. Nasir, A. Zingale, E. Chowdhury, B. F. Shen, and D. W. Schumacher, Phys. Plasmas **26**, 033110 (2019).

[60] J. Williams (private communication).

[61] A. Haid, L. Carlson, N. Alexander, B. Russ, A. Forsman, J. Oakdale, and S. Chenen, Poster presentation in the 2019 Target Fabrication Conference: https://tfab19.lle.rochester.edu/

[62] J. Williams, private communications at General Atomics, 2019.

[63] A. Haid, L. Carlson, N. Alexander, B. Russ, A. Forsman, J. Oakdale, and S. Chenen, Millimeter-scale seamless 2-photon polymerization additive manufacturing, poster presentation in the 2019 Target Fabrication Conference, https://tfab19.lle.rochester.edu/

[64] T. Arber, K. Bennett, C. Brady, A. Lawrence-Douglas, M. Ramsay, N. Sircombe, P. Gillies, R. Evans, H. Schmitz, A. Bell *et al.*, Plasma Phys. Controlled Fusion **57**, 113001 (2015).

[65] H. Alfvén, Phys. Rev. **55**, 425 (1939).

[66] M. Tatarakis, F. N. Beg, E. L. Clark, A. E. Dangor, R. D. Edwards, R. G. Evans, T. J. Goldsack, K. W. D. Ledingham, P. A. Norreys, M. A. Sinclair, M. S. Wei, M. Zepf, and K. Krushelnick, Phys. Rev. Lett. **90**, 175001 (2003).

[67] C. M. Huntington, A. G. R. Thomas, C. McGuffey, T. Matsuoka, V. Chvykov, G. Kalintchenko, S. Kneip, Z. Najmudin, C. Palmer, V. Yanovsky, A. Maksimchuk, R. P. Drake, T. Katsouleas, and K. Krushelnick, Phys. Rev. Lett. **106**, 105001 (2011).

[68] P. Auer, Phys. Fluids **17**, 148 (1974).

[69] I. Dodin and N. Fisch, Phys. Plasmas **13**, 103104 (2006).

[70] T. Wang, Z. Gong, K. Chin, and A. Arefiev, Plasma Phys. Controlled Fusion **61**, 084004 (2019).

[71] L. D. Landau and E. M. Lifshitz (unpublished).

[72] A. Di Piazza, K. Z. Hatsagortsyan, and C. H. Keitel, Phys. Rev. Lett. **102**, 254802 (2009).

[73] M. Tamburini, F. Pegoraro, A. Di Piazza, C. H. Keitel, and A. Macchi, New J. Phys. **12**, 123005 (2010).

[74] A. G. R. Thomas, C. P. Ridgers, S. S. Bulanov, B. J. Griffin, and S. P. D. Mangles, Phys. Rev. X **2**, 041004 (2012).

[75] J.-X. Li, K. Z. Hatsagortsyan, and C. H. Keitel, Phys. Rev. Lett. **113**, 044801 (2014).

[76] T. G. Blackburn, C. P. Ridgers, J. G. Kirk, and A. R. Bell, Phys. Rev. Lett. **112**, 015001 (2014).

[77] A. Gonoskov, A. Bashinov, I. Gonoskov, C. Harvey, A. Ilderton, A. Kim, M. Marklund, G. Mourou, and A. Sergeev, Phys. Rev. Lett. **113**, 014801 (2014).

[78] J. M. Cole, K. T. Behm, E. Gerstmayr, T. G. Blackburn, J. C. Wood, C. D. Baird, M. J. Duff, C. Harvey, A. Ilderton, A. S. Joglekar, K. Krushelnick, S. Kuschel, M. Marklund, P. McKenna, C. D. Murphy, K. Poder, C. P. Ridgers, G. M. Samarin, G. Sarri, D. R. Symes, A. G. R. Thomas, J. Warwick, M. Zepf, Z. Najmudin, and S. P. D. Mangles, Phys. Rev. X **8**, 011020 (2018).

[79] K. Poder, M. Tamburini, G. Sarri, A. Di Piazza, S. Kuschel, C. D. Baird, K. Behm, S. Bohlen, J. M. Cole, D. J. Corvan, M. Duff, E. Gerstmayr, C. H. Keitel, K. Krushelnick, S. P. D. Mangles, P. McKenna, C. D. Murphy, Z. Najmudin, C. P. Ridgers, G. M. Samarin, D. R. Symes, A. G. R. Thomas, J. Warwick, and M. Zepf, Phys. Rev. X **8**, 031004 (2018).

[80] T. N. Wistisen, A. Di Piazza, H. V. Knudsen, and U. I. Uggerhøj, Nat. Commun. **9**, 795 (2018).

[81] F. Mackenroth and A. Di Piazza, Phys. Rev. A **83**, 032106 (2011).

[82] A. Di Piazza, C. Müller, K. Z. Hatsagortsyan, and C. H. Keitel, Rev. Mod. Phys. **84**, 1177 (2012).

[83] N. Neitz and A. Di Piazza, Phys. Rev. Lett. **111**, 054802 (2013).

[84] F. Mackenroth and A. Di Piazza, Phys. Rev. Lett. **110**, 070402 (2013).

[85] T. G. Blackburn, A. Ilderton, M. Marklund, and C. P. Ridgers, New J. Phys. **21**, 053040 (2019).

[86] P. Zhang, S. S. Bulanov, D. Seipt, A. V. Arefiev, and A. G. R. Thomas, Phys. Plasmas **27**, 050601 (2020).

[87] A. Arefiev, Z. Gong, and A. P. L. Robinson, Phys. Rev. E **101**, 043201 (2020).

[88] T. Wang, Z. Gong, and A. Arefiev, Phys. Plasmas **27**, 053109 (2020).

[89] A. Gonoskov, A. Bashinov, S. Bastrakov, E. Efimenko, A. Ilderton, A. Kim, M. Marklund, I. Meyerov, A. Muraviev, and A. Sergeev, Phys. Rev. X **7**, 041003 (2017).

[90] Z. Gong, F. Mackenroth, X. Yan, and A. Arefiev, Sci. Rep. **9**, 17181 (2019).